Jet Calibration and Systematic Uncertainties for Jets Reconstructed in the ATLAS Detector at $\sqrt{s} = 13$ TeV

The ATLAS Collaboration

Abstract

This document describes the calibration of $R = 0.4$ anti-k_t jets reconstructed in the ATLAS detector at a center-of-mass energy of 13 TeV. It also describes how systematic uncertainties on the jet energy scale and resolution have been derived exploiting knowledge acquired during Run 1 combined with detailed studies using Monte Carlo simulations. The full set of systematic uncertainties is presented for jets in the fiducial region of the detector with pseudorapidity $|\eta| < 0.8$. These uncertainties vary from 6% for jets with transverse momentum $p_T = 20$ GeV, decreasing to 1% for jets of $p_T = 200 - 1800$ GeV and increasing again to 3% for jets of higher p_T, for the average pile-up conditions expected during the 2015 data-taking period. Uncertainties on the jet energy resolution and those related to pile-up are derived for the full η range of the detector.

1 Introduction

Early measurements and searches, using the first data gathered in 2015 by ATLAS [1] at a center-of-mass energy of 13 TeV require calibrated jets before enough data is available to perform dedicated *in situ* studies of the jet energy scale and resolution [2]. One can take advantage of the significant similarity of the detector, conditions, and Monte Carlo (MC) simulations between Run 1 and Run 2 to provide jet calibrations and systematic uncertainties based on Run 1 MC and data-based calibrations. Comparisons of MC simulations implementing individual changes to detector and run conditions between Run 1 and Run 2 are used to measure their impact on the jet energy scale and jet energy resolution.

This document is structured as follows: Section 2 describes the ATLAS detector and aspects of the detector signal processing relevant to the studies shown. Section 3 describes the jet reconstruction algorithms, focusing on aspects that have been updated for Run 2. Section 4 summarizes the details of the changes in the ATLAS detector, data-taking conditions, jet reconstruction and MC simulation going from 2012 to 2015. Understanding these changes and their effect on the jet energy scale and resolution is critical to the use of studies on 2012 data in establishing the uncertainties on jets reconstructed in 2015 data. Section 5 describes the MC simulations used to gain this understanding and Sec. 6 describes how the jet kinematics are calibrated in 2015 MC simulations and data. Finally, Sec. 7 shows how the systematic uncertainties are derived for jets reconstructed in 2015 data.

2 The ATLAS Detector

The ATLAS detector provides nearly full solid angle coverage around the collision point with an inner tracking system covering the pseudorapidity[1] range $|\eta| < 2.5$, electromagnetic (EM) and hadronic calorimeters covering $|\eta| < 4.9$, and a muon spectrometer covering $|\eta| < 2.7$. The inner detector (ID) is comprised of 3 subdetectors layered radially in the central region: a silicon pixel tracker closest to the beamline, a microstrip silicon tracker, and a straw-tube transition radiation tracker at radii up to 108 cm. A thin solenoid surrounding the tracker provides an axial 2 T field enabling the measurement of charged particle momenta. For Run 2, a new, innermost layer of the silicon pixel tracker, called the insertable B-layer (IBL), has been inserted at a radial distance of 3.3 cm from the beam line [3] to improve charged-particle reconstruction in the new environment among an increased number of proton-proton collisions within a given bunch crossing (*in-time pile-up*).

The high-granularity EM and hadronic calorimeters are composed of multiple sub-detectors spanning $|\eta| < 4.9$. The EM barrel calorimeter uses a liquid argon (LAr) active medium and lead absorbers. In the region $|\eta| < 1.7$, the hadronic (Tile) calorimeter is constructed from steel absorber and scintillator tiles and is separated into barrel ($|\eta| < 1.0$) and extended barrel ($0.8 < |\eta| < 1.7$) sections. The calorimeter end-cap ($1.375 < |\eta| < 3.2$) and forward ($3.1 < |\eta| < 4.9$) regions are instrumented with LAr calorimeters for both EM and hadronic energy measurements. The LAr barrel has three longitudinal EM layers (EM1, EM2, EM3), the LAr end-cap has three EM layers (EMEC1, EMEC2, EMEC3) and four hadronic layers

---

[1] The ATLAS coordinate system is a right-handed system with the x-axis pointing to the center of the LHC ring and the y-axis pointing upwards. The polar angle θ is measured with respect to the LHC beam-line. The azimuthal angle ϕ is measured in the transverse (xy) plane with respect to the z-axis. The pseudorapidity η is an approximation for rapidity y in the high energy limit, and it is related to the polar angle θ as $\eta = -\ln\tan(\frac{\theta}{2})$. The rapidity is defined as $y = 0.5 \times \ln[(E + p_z)/(E - p_z)]$, where E denotes the energy and p_z is the component of the momentum along the beam direction. Transverse momentum and energy are defined as $p_T = p \times \sin(\theta)$ and $E_T = E \times \sin(\theta)$, respectively.

(HEC1, HEC2, HEC3, HEC4), and the forward LAr calorimeter has three layers (FCal1, FCal2, FCal3). The Tile calorimeter has three longitudinal layers (Tile1, Tile2, Tile3) as well as scintillators in the gap region spanning ($0.85 < |\eta| < 1.51$) between the barrel and extended barrel sections. In addition, there is a pre-sampler (PS) layer in front of the LAr electromagnetic calorimeter within $|\eta| < 1.8$ that is used to get a measure of the energy deposited by particles in non-instrumented material in front of the EM calorimeter.

The analog signals of the LAr detector are sampled digitally once per bunch crossing over 4 bunch crossings and those measurements are converted to an energy measurement using constants calculated using dedicated calibration runs [1, 4]. During the 2012 data-taking period, 5 samples instead of 4 were used in the LAr calorimeters energy measurement. The LAr readout is sensitive to signals from the preceding 12 bunch crossings during 50 ns bunch spacing operation [1, 4]. For the 25 ns bunch spacing scenario this increases to 24 bunch crossings. The LAr detector will thus be exposed to more *out-of-time pile-up* in most of the 2015 run. In contrast, the fast readout of the Tile calorimeter makes it relatively insensitive to out-of-time pile-up [5, 6].

The muon spectrometer surrounds the ATLAS calorimeters. A system of three large air-core toroids, a barrel and two endcaps, generates a magnetic field in the pseudorapidity range of $|\eta| < 2.7$. The muon spectrometer measures muon tracks with three layers of precision tracking chambers and is instrumented with separate trigger chambers.

The trigger system for the ATLAS detector consists of a hardware-based Level 1 (L1), as well as software-based higher-level trigger [7]. The aforementioned change in the number of samplings used to reconstruct energy deposits in the LAr calorimeters has been commissioned in order to allow for the L1 trigger to accept data at a rate of 100 kHz in Run 2 [8].

3 Reconstruction and Event Selection

Jets in the ATLAS calorimeters are reconstructed using the anti-k_t algorithm [9] with radius parameter $R = 0.4$, using as input positive-energy topological clusters (topoclusters) [10] of calorimeter cell energies. The three-dimensional topoclusters are built from topologically connected calorimeter cells that contain a significant signal above noise. The simulated noise-levels used in the calibration of the topocluster recontruction algorithm have been changed for 2015 with respect to those used in 2012 to better match noise levels observed in 2012 data. Those changes are at the level of 10% in the barrel region of the detector and somewhat larger in the forward region. The cluster reconstruction algorithm itself has undergone small modifications for the processing of 2015 with respect to that used for 2012 data. Specifically, clusters are forbidden from growing from the PS layers of the calorimeter using neighbors in those same layers. This prevents low-energy pile-up energy depositions that only reach the PS from creating large clusters dominated by pile-up noise.

The studies in this note are made with jets reconstructed from topoclusters at the electromagnetic (EM) energy scale, which correctly measures the energy deposited by electromagnetic showers in the calorimeter [10]. While this document limits its scope specifically to anti-k_t $R = 0.4$ jets built from EM topoclusters, the methodology demonstrated herein may readily be applied to other reconstructed jets used in Run 1, such as jets built with topoclusters calibrated with the local cluster weighting calibration [11].

For studying the jet calibration, *truth jets* are built in MC simulation using as inputs simulated particles with a lifetime τ, defined by $c\tau > 10$ mm, that are neither final-state muons nor neutrinos. Muons and neutrinos are ignored in truth jet reconstruction as they leave little or no visible energy in the calorimeters.

Tracks of charged particles used in the jet calibration are reconstructed within the full acceptance of the ID, $|\eta| < 2.5$. Reconstructed tracks are required to have transverse momentum of at least 500 MeV, be used in the primary vertex fit or be tightly associated to it, and satisfy a number of loose quality criteria relating to the number of hits in the different ID sub-detectors. Tracks are associated to jets using *ghost association* [12] that treats them as 4-vectors of infinitesimal magnitude during jet reconstruction.

Track reconstruction has been updated in 2015 not only for the inclusion of the IBL, but also to better separate hits merged due to the proximity of two tracks and increase algorithm speed in the high luminosity conditions expected in Run 2 [13]. The quality criteria listed above have been optimized based on MC simulations. Early data studies [14] have demonstrated that the agreement between 2015 data and MC simulations is comparable to that obtained in 2012 data [15].

Muon track segments are used as part of the jet calibration procedure as a proxy for the uncaptured jet energy carried by energetic particles passing through the calorimeters without being fully absorbed. The segments used are partial tracks constructed from hits in the muon spectrometer [16] that are used as the input to fully reconstructed tracks. These segments are associated to jets using the method of ghost association described above for tracks where the global position of the segment is used as the position vector in the ghost association procedure. Muon segment reconstruction has been updated in 2015 as described in Sec. 4.

3.1 Jet selection

Except for the calculation of pile-up related quantities, an inclusive selection of jets is made with the following prescription: Reconstructed calorimeter jets are matched geometrically to truth jets within $\Delta R = \sqrt{(\eta_{\text{calo}} - \eta_{\text{truth}})^2 + (\phi_{\text{calo}} - \phi_{\text{truth}})^2} < 0.3$. Only "isolated" jets are used in this document to avoid any ambiguities in the matching of calorimeter jets to truth jets. The isolation requirement for calorimeter jets is that there should be no other calorimeter jet of $p_{\text{T}} > 5$ GeV (at the scale obtained after $\rho \times A$ subtraction, described in Sec. 6.1) within $\Delta R = 1.0$, and only one truth jet with $p_{\text{T}}^{\text{truth}} > 7$ GeV within a cone of $\Delta R = 0.6$. For pile-up studies the matching of truth jets with reconstructed jets is made without isolation requirements within $\Delta R < 0.4$, where any ambiguity is resolved by taking the closest match in ΔR.

For flavor studies in MC simulation, the labeling of the flavor of a jet is done by geometrically matching the jet with the generator level hadrons/partons: if a b-hadron is found within $\Delta R < 0.3$ of the jet direction, the jet is labelled as a b-jet. If no b-hadron is found, the procedure is repeated for c-hadrons. If no such association can be made then the highest-energy parton from the event generator within $\Delta R < 0.4$ to the jet determines its flavor. This definition is sufficient to study the flavor dependence of the calorimeter response to jets [17]. Any theoretical ambiguities of jet flavor assignment are not relevant in this context.

Throughout this document, the average calorimeter response to jets, or average jet p_{T} response, for a given population of calorimeter jets is defined as $R = \langle p_{\text{T}}^{\text{jet}} / p_{\text{T}}^{\text{truth}} \rangle$, where $p_{\text{T}}^{\text{jet}}$ is the calorimeter jet p_{T} and $p_{\text{T}}^{\text{truth}}$ is the p_{T} of the matched truth jet. The mean is taken from a Gaussian fit to the $p_{\text{T}}^{\text{jet}} / p_{\text{T}}^{\text{truth}}$ distribution within a range of 1.6σ from its mean value. For certain applications the jet *energy response* is used, which is defined similarly but using the energies instead of the transverse momenta. The jet resolution, σ_R, is

defined by the standard deviation of the Gaussian fit to the jet response distribution. The fractional jet resolution ($\sigma_R/R = \sigma_{p_T}/p_T$) is used to determine the size of the fluctuations in the jet p_T reconstruction.

4 Summary of Changes from Run 1 to Run 2

A number of changes between Run 1 and Run 2 are relevant to the calibration of jets in ATLAS. These include changes to the beam conditions, ATLAS detector, simulation, and the reconstruction of analysis objects. Some of these changes have already been discussed in the previous sections. This section summarizes these changes and their potential impact on the jet calibration. How each of these changes impact the calibration or its systematic uncertainties is discussed in detail in Secs. 6 and 7.

Detector A new detector, the IBL, has been installed. The amount of material added in the central region of the detector is a fraction of the total pixel detector, and corresponds to about 0.04 radiation lengths (X_0) [3]. This is about 0.2% of the total amount of material in the EM calorimeter, and its impact on the jet response is considered to be comparably negligible. The amount of material due to read-out services for the IBL is, however, large and highly modulated in ϕ for $|\eta| > 3.5$, adding up to 5 X_0 near $|\eta| \approx 4.5$. Additional changes to the subdetectors and material distributions are limited to small upgrades and are not significant to the early calibration of jets.

Beam conditions Three changes in beam conditions have the potential to affect the calibration of jets in 2015 data: the center of mass energy of the collisions, the bunch spacing, and the luminosity distribution. The center of mass energy is increased from $\sqrt{s} = 8$ TeV in 2012 to $\sqrt{s} = 13$ TeV in 2015. This is expected to impact the jet calibration through a change in the quark/gluon fraction of the calibration sample and a change in the underlying event and pile-up contributions. The change in the flavor composition of the calibration sample has no impact on systematic uncertainties, since dedicated uncertainties for flavor effects already exist. The change in the underlying event is subdominant with respect to the effect of pile-up contributions. The proton bunch spacing within trains is halved from 50 ns to 25 ns, for a large fraction of the year, which doubles the amount of out-of-time pile-up. The detector read-out, however, is optimized for this change, which leads to the expectation that the effect fo this is small. The average luminosity is expected to be similar in 2015 to that achieved during 2012 data taking. Three main periods of data will be taken during 2015, with the following rough goals for each: less than 1 fb^{-1} integrated luminosity at 50 ns bunch spacing with a target $\langle\mu\rangle$ of 25, 5 fb^{-1} at 25 ns bunch spacing with a target $\langle\mu\rangle$ of 21, and 4 fb^{-1} at 25 ns bunch spacing with a target $\langle\mu\rangle$ of 35.

LAr calorimeter energy reconstruction The timing and energy of the LAr calorimeter in 2012 were reconstructed using a linear combination of 5 sampling points as described in Ref. [4]. The optimal filter coefficients (OFCs) for this calculation are calculated with dedicated runs where the signal pulse shape is injected into the detector with the time distribution expected for a specific luminosity and bunch structure. In 2015, the calculation uses only 4 sampling points and the OFCs have been calibrated on 25 ns bunch spacing. The same OFCs are used when taking data at 50 ns bunch spacing, but dedicated corrections are applied to correct the energy of each individual cell for biases caused by the lack of dedicated OFCs.

Topocluster reconstruction As discussed in Sec. 3, noise-levels defined for the calibration of the topoclustering algorithm in 2015 have changed with respect to those used in 2012 in order to better match noise measurements made in 2012 data. In addition, in 2015, topoclusters are forbidden from growing from the PS layers of the calorimeter using neighbors in those same layers. This mitigates the impact of pile-up on jet reconstruction.

Muon track segments Muons reconstructed in the muon spectrometer are seeded by segments reconstructed from adjacent hits in the monitored drift tubes. Drift times in individual drift tubes are matched temporally to seed the reconstruction of a segment. Due to the combinatoric nature of the muon reconstruction algorithm the timing thresholds have been tightened in the initial seeding of muon segments in 2015 to reduce the CPU consumption of muon reconstruction. In addition, the procedure of associating segments to jets has moved from an $\eta - \phi$-cone to a ghost association process similar to that of ID track association as mentioned in Sec. 3. Consequently there is better matching to the geometrical extension of the jet. All these changes significantly change the number of segments reconstructed behind a jet. Since this number is used in the jet calibration as a proxy for the amount of energy from the jet not contained in the calorimeter, a significant change in the number does not lead to a change in the systematic uncertainties in the calibration, as long as the calibration constants are updated.

Track reconstruction As discussed in Sec. 3, track reconstruction has been updated in 2015 for the inclusion of the IBL, to better separate hits merged due to the proximity of two tracks and to increase its speed [13]. Tracks are used in the jet calibration as proxies for the jet fragmentation. Given that they remain good proxies and the calibration constants are updated, small changes in the quantities used in the jet calibration will not significantly impact the estimate of systematic uncertainties.

Detector simulation The simulation of the inelastic scattering of hadrons of up to 10 TeV on detector materials has changed from the combination of 3 models to 2 models, the combinations known respectively as QGSP_BERT and FTFP_BERT [18]. In 2012 analyses, the Bertini cascade model was used for hadrons with $E < 9.9$ GeV, a GEISHA-based low energy parameterized model for hadrons with $9.5 < E < 25$ GeV, and QGSP in the range above 12 GeV. In 2015 simulations, the higher energy range, above 4 GeV, is covered by the FTFP model, and the Bertini cascade model is used only up to 5 GeV, where studies have shown a smooth response in the transition region between the two models [18]. Additionally, the response of the Tile calorimeter cells to particles was found to be dependent on the azimuthal position with respect to the cell center. This dependence was not modeled in Run 1 MC simulations, but is now modeled in the simulations of 2015 data. This change in modeling leads also to an overall change in the scale of energy reconstructed in the Tile calorimeter. Finally, the detector simulation and reconstruction have been updated to represent all the changes summarized in this section.

5 Monte Carlo Simulations

The simulation of *pp*-collisions in the ATLAS detector used in jet calibration and evaluation of the related systematic uncertainties has been performed using one MC generator, except in the derivation of generator-based uncertainties. A *nominal sample* of dijet events, reflecting our best knowledge of 2015

data-taking conditions, is simulated using Pythia 8 [19], with the A14 [20] underlying event tune and the NNPDF23LO [21] parton density function set (PDF).

The pile-up effects are modeled using simulated minimum bias events generated also using Pythia 8 with the A14 tune and the NNPDF23LO PDF. These events are overlaid onto the hard-scatter events following a Poisson distribution around the average number of additional pp collisions per bunch crossing, μ, expected in the 2015 data-taking period both in time with the simulated hard scatter and for previous bunches with 25 ns spacing. The μ distribution used in the simulation of the samples in this document is shown in Fig. 1. The effects from pile-up events occurring in nearby bunch crossings (out-of-time pile-up) are
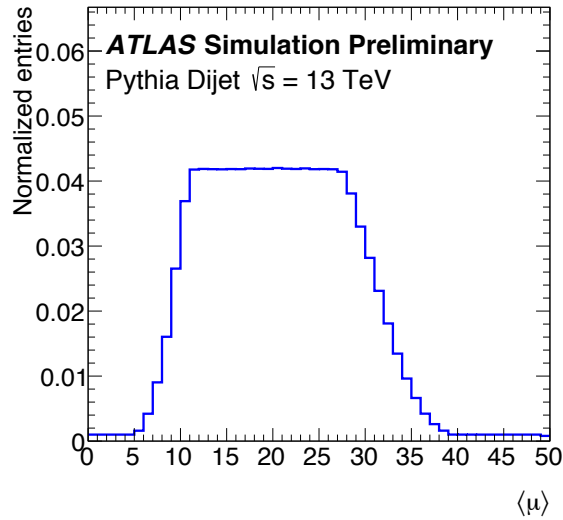

Figure 1: Distribution of average number of pile-up interactions overlaid with the hard-scatter in MC simulations.

also modeled by overlaying the hard-scatter event with simulated detector signals from Pythia 8 minimum bias events. These overlaid events are sampled from out-of-time bunches according to a simulation of the expected LHC bunch train structure during 25 ns data-taking periods.

Generated events are propagated through a full simulation of the ATLAS detector [22] based on Geant4 [23] that simulates the interactions of the particles produced by the event generators with the detector material. Hadronic showers are simulated with the FTFP_BERT model.

In addition to this *nominal sample*, a *reference sample* and several additional samples were produced at a preliminary stage in the software developement with specific changes in the conditions or the detector simulation in order to understand how each individual change undergone between Run 1 and Run 2 affects jet energy scale, jet resolution, and to attribute a systematic uncertainty associated with each. These additional samples have been produced at a preliminary stage in the MC developement to allow time for analysis prior to their application at the arrival of first data. Most of these samples are generated with the Pythia 8 generator using the CT10 PDFs [24] with the AU2 underlying event tune and do not include a simulation of the ϕ-dependent response within the Tile calorimeter cells. In addition, the simulation of the services of the IBL in the forward region of the detector is simulated as being uniform, in contrast with the nominal detector simulation above, for which a modulation in ϕ is introduced to more accurately represent the bundling of services. Exceptions are mentioned explicitly in what follows.

- *Reference sample.* As the nominal sample except it is using CT10 PDFs with the AU2 UE tune, no ϕ-dependent tile response, no ϕ-modulation of the IBL services in the forward region, exactly as mentioned above. The reference sample is used in place of the nominal sample for comparison with the following group of variants that have been produced with conditions defined in a software release preceding that of the production of the nominal sample to isolate the effect of the specific variations made.

- *Tile ϕ-dependent response off.* As the nominal sample, except the ϕ-dependent response of the Tile calorimeter cells, which is not simulated.

- *QGSP BERT.* As the reference sample, but using QGSP_BERT to model hadronic showers, as in 2012 simulations.

- *Run 1 topoclustering.* As the reference sample, but allows topocluster growth from the PS layer as in 2012 reconstruction.

- *Variation of noise thresholds.* As the reference sample but with noise thresholds used in the topoclustering shifted up and down by a fraction consistent with the discrepancy observed between data and MC simulations in 2012 data.

- *50 ns with 5 sampling points in the LAr calorimeter..* As the reference sample, but using a bunch spacing of 50 ns, and 5 sampling points in the LAr calorimeter energy reconstruction, with corresponding OFCs. This sample reproduces the data-taking conditions of the LAr calorimeters used in 2012.

- *50 ns with 4 sampling points in the LAr calorimeter.* As the reference sample, but using a bunch spacing of 50 ns, and 4 sampling points in the LAr calorimeter energy reconstruction, with corresponding OFCs. This sample, when compared to the reference sample and the 50 ns/5-sampling points sample, allows decoupling the effects of the change in bunch spacing from those related to the change in the number of read-out sampling points.

- *Early 2015 data-taking conditions.* As the reference sample, but using the read-out settings that will be used in the early part of the 2015 run, with 50 ns bunch spacing. This sample is different from the ones above in that the OFCs are the same as those used for the 25 ns part of the run, as described in more detail in Sec. 4.

- *Modulated forward IBL geometry.* As the reference sample, but with the same geometry as that of the nominal sample.

- *Herwig++.* As the reference sample, but using the Herwig++ generator [25] with the CTEQ6 PDF and the UE-EE-4 underlying event tune to generate the hard-scatter events.

How each of these samples is used is described in detail in Secs. 6 and 7, but, for reference Tab. 1 summarizes the changes in each sample and in which sections their usage is discussed.

6 Jet Calibration

The calibration procedure used in 2015 is the same as that used in 2012, detailed in Ref. [26]. First, a jet is corrected to point back to the identified hard-scatter vertex. Next, the effect of pile-up is removed using an area-based subtraction procedure and residual corrections discussed in Sec. 6.1. The jet energy is then

Sample	Diff. with reference	Usage
Nominal	PDF, UE tune, tile sim., forward geo.	Calibration (Sec. 6)
Reference		Calibration (Sec. 6), unc. (Sec. 7)
Tile response	PDF, UE tune	Calibration (Sec. 6), unc. (Sec. 7.1)
QGSP BERT	Hadronic physics list	Calibration (Sec. 6.4)
Topoclustering	Adjusted Algorithm	Uncertainties (Sec. 7.1)
Noise thresholds	Refined by 2012 data	Uncertainties (Sec. 7)
50 ns/5-sampling	Bunch spacing, LAr reco.	Uncertainties (Sec. 7)
50 ns/4-sampling	Bunch spacing, LAr reco.	Uncertainties (Sec. 7)
Early data	Bunch spacing, LAr reco.	Uncertainties (Sec. 7)
IBL geometry	Forward geometry	Uncertainties (Sec. 7)
Herwig++	Generator, PDF, UE tune	Uncertainties (Sec. 7.3)

Table 1: Summary of different dijet samples produced. Column 2 indicates the nature of the difference between each sample produced and the reference sample. Column 3 shows how each sample is used within this note.

calibrated by applying a p_T and η-dependent correction derived from the nominal 2015 MC simulation. At this step, biases in the η position of the jets, caused by the different calorimeter technologies in different η regions, are also corrected. Both these corrections are described in Sec. 6.2. In addition to these steps, further corrections are applied to the jets that reduce the dependence of the jet energy measurement on the longitudinal and transverse structure of the jets and also correct for jets that are not fully contained in the calorimeter. These corrections are described in Sec. 6.3. Finally, for jets in the data, an additional correction is applied that changes their calibration to its correct value based on in situ studies performed in 2012 [26]. These corrections are applicable to 2015 data, as long as changes in the detector and conditions are modeled in the MC simulation and the uncertainties in that modeling are considered as part of the systematic uncertainties. The calibration of jets has been made in the full η acceptance of the detector up to the derivation of the in situ correction which has been limited only to the $|\eta| < 0.8$ region in anticipation of its use in 2015 data-driven studies that extend the in situ correction to the rest of the detector [27]. Further details of the derivation of the insitu correction are found in Sec. 6.4.

6.1 Pile-up corrections

To reduce the effects of pile-up on jet calibration, an area-based subtraction method is employed [28]. This removes the effect of pile-up utilizing the average energy density in the $\eta \times \phi$ plane, ρ, and the area of the jet in this plane, A, where it has been calculated by ghost association. The area of a jet is calculated using an active areas algorithm in which ghost particles of infinitesimal momentum are uniformly added to the event before jet clustering. The number of ghosts clustered into each jet then gives a measure of the area of the jet. The pile-up energy density of the event is calculated using k_t, R = 0.4 jets reconstructed in the central ($|\eta| < 2.0$) region of the detector. The energy density of each jet is defined as p_T/A and

the event ρ then found from the median energy density of these jets. The ρ distribution for events with different numbers of primary vertices, N_{PV}, in 2015, 25 ns MC simulation is shown in Fig. 2.
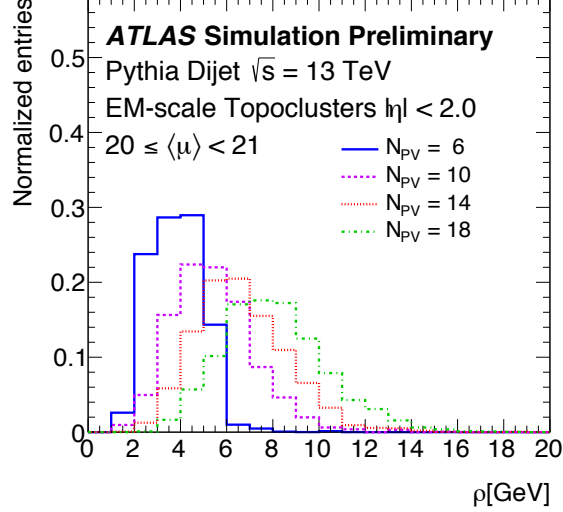

Figure 2: Event p_T density, ρ, for an average number of interactions $20 \leq \langle\mu\rangle < 21$, for four different values of N_{PV} in 25 ns, 13 TeV MC dijet simulation. ρ is calculated from jets with $|\eta| < 2.0$.

It is observed that after this correction some dependence of the jet p_T on pile-up remains, so an additional residual correction is applied as a function of N_{PV} and the average number of interactions per bunch crossing, $\langle\mu\rangle$, such that both residual in-time and out-of-time effects can be captured. The pile-up subtracted p_T following area-based correction and residual correction, p_T^{corr}, is therefore given by:

$$p_T^{corr} = p_T^{EM} - \rho \times A - \alpha \times (N_{PV} - 1) - \beta \times \langle\mu\rangle, \tag{1}$$

where α and β are derived from the residual dependence in the nominal MC sample, parameterized by η, and define the residual correction. The fit providing these constants is shown in Fig. 3 and applied as a correction in the last step. The successful removal of the residual pile-up effects on the jet p_T achieved by this correction is also illustrated in Fig. 3. It should be noted that the out-of-time pile-up residual effects in the forward region are larger in 2015 MC simulations than what was found in 2012 MC simulations [28]. This is likely caused by a combination of changes in the read-out, noise thresholds and amount of out-of-time pile-up, and is explored in more detail in Sec. 7.2.

6.2 Jet energy scale and η corrections

The jet energy scale calibration is derived as a correction that relates the reconstructed jet energy to the truth jet energy [29]. The jet energy scale factors are derived from isolated jets (see Sec. 3.1) from an inclusive dijet MC simulation after correcting the jets for the position of hard-scatter vertex and applying the pile-up corrections. Figure 4(a) shows the average energy response, which is the inverse of the jet calibration factor. Gaps and transitions between sub detectors of the calorimeter result in a lower energy response, evident when parameterized in η, as a result of absorbed or undetected particles.
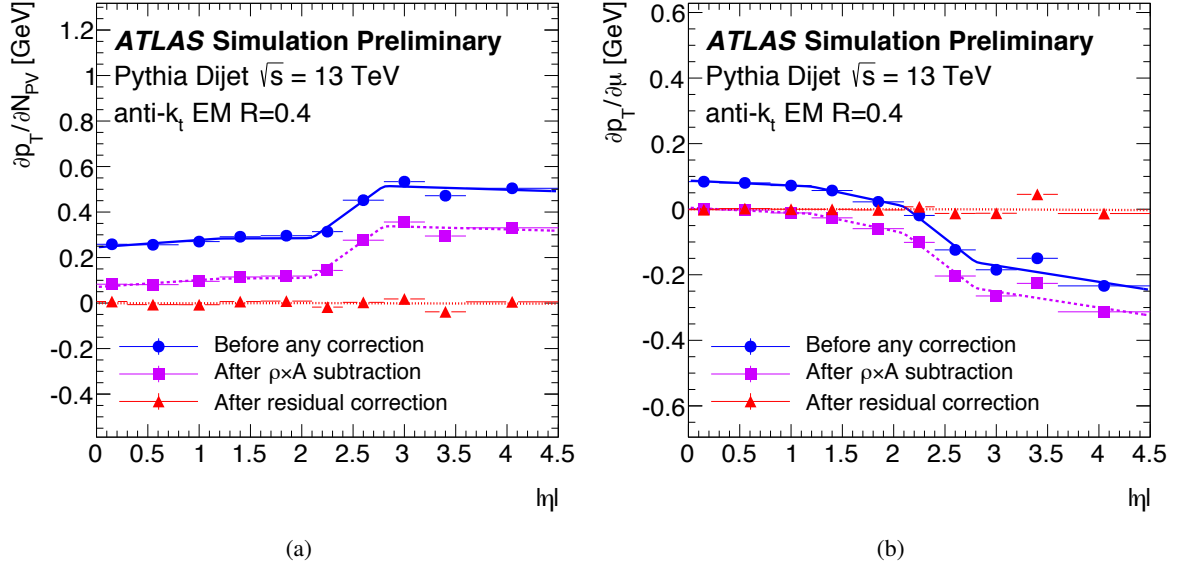
(a)   (b)

Figure 3: Dependence of the reconstructed jet p_T on in-time pile-up (a) and out-of-time pile-up (b) at various correction stages in bins of jet $|\eta|$ shown with the piecewise linear fit used to define the residual correction. The red curve shows the application of the residual corrections α in a) and β in b).
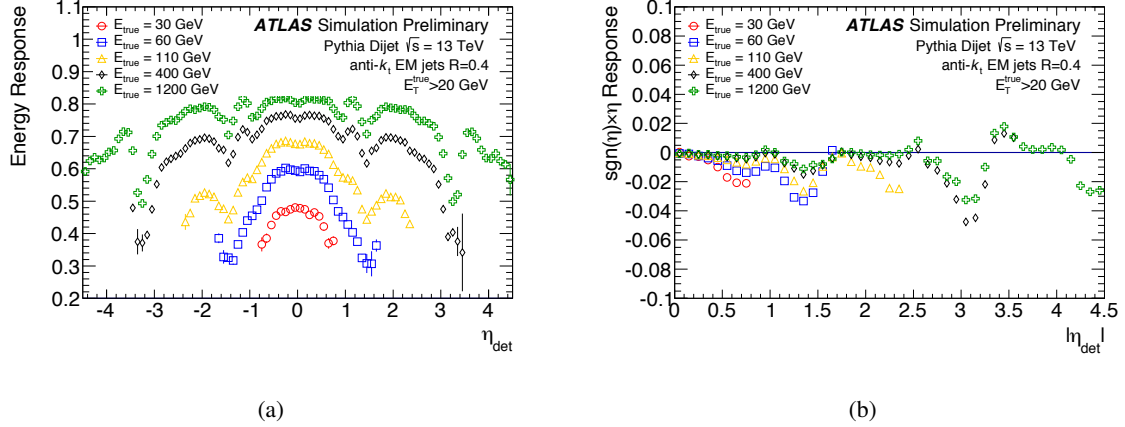

(a)   (b)

Figure 4: Energy response (a) and bias in the η reconstruction (b) as a function of η before calibration for EM scale anti-k_t, R=0.4 jets.All pile-up corrections have been applied, as well as for the position of the hard scatter vertex.

Following the calibration in energy it is found that in specific regions of the detector there is a bias in the reconstruction of the η direction of the jet. An additional correction in η is applied to resolve this bias. It is antisymmetric and shown as a function of $|\eta|$ in Fig. 4(b). This bias is also visibly affected by the gaps and transitions in the calorimeters and its correction brings the average reconstructed p_T of jets closer to their truth value.

11

6.3 Global sequential corrections

Following the above jet calibration scheme, it is observed that there is a dependence of the jet energy scale on longitudinal and transverse features of the jet. This dependence is corrected sequentially, benefiting from the largely uncorrelated nature of the effects captured by each correction. An additional correction that uses the same methodology is applied at the end to reduce tails in the response distribution caused by jets that are not fully contained in the calorimeter at high p_T. The five stages of the correction correct for the dependence of the jet energy on (in order):

1. the fraction of energy deposited in the first layer of the Tile calorimeter,

2. the fraction of energy deposited in the third layer of the electromagnetic calorimeter,

3. the number of tracks associated to the jet as described in Sec. 3,

4. the p_T-weighted width of the tracks associated to the jet as described in Sec. 3,

5. the number of muon segments associated to the jet as described in Sec. 3.

Further details of the global sequential corrections can be found in Ref. [15]. The dependence exploited by these corrections is illustrated in Fig. 5 for some of these variables. The variables used in these corrections have been studied using 2015 data and the nominal MC simulation [14]. The agreement between data and the MC simulation is comparable to that found using 2012 data [15].

6.4 In situ corrections

The final in situ corrections account for differences between data and MC simulation in the jet p_T measurement. Such differences can originate from limitations in the simulation of the underlying event, physics of jet formation, pile-up activity, the physics of electromagnetic and hadronic interactions in the detector, and the description of the detector material. The corrections are calculated using γ/Z+jet and multijet processes in 2012 data and MC simulations [2, 15, 26, 30]. In each of those analyses the ratio of p_T between a jet and reconstructed reference object ($r = p_\mathrm{T}^\mathrm{jet}/p_\mathrm{T}^\mathrm{ref}$) is built, and compared between data and MC. The ratio $f_{2012} = r_{2012}^\mathrm{MC}/r_{2012}^\mathrm{data}$, then makes up the in situ correction to be applied to data, such that the calibrated jet p_T in 2012 data is:

$$p_\mathrm{T}^\mathrm{corr} = f_{2012}(p_\mathrm{T}, \eta) \times C_{2012}(p_\mathrm{T}^\mathrm{EM}, \eta, N_{PV}, \mu, \{g_i\}) \times p_\mathrm{T}^\mathrm{EM}, \tag{2}$$

where $\{g_i\}$ refer to the variables defined in Sec. 6.3 and C_{2012} captures all the corrections described in Secs. 6.1, 6.2 and 6.3 as calculated for 2012 data analyses. In this way, the calibration applied to the data is $f_{2012} \times C_{2012}$, and for MC is just C_{2012}.

To first order, $f_{2012} \times C_{2012}$ does not require an update for 2015 data taking, because the changes in the detector in the central region are limited to the very small amount of material added by the IBL there. Based on this, it is justified to use f_{2012} in 2015 data with some additional considerations on systematic effects that can arise from the different pile-up conditions and underlying event, as well as the changes in the read-out settings of the relevant detectors. These systematic effects are discussed further in Sec. 7.

However, as described in previous sections, C_{2015} has been recalculated using updated MC simulations that will be used in 2015 data analyses. These updated simulations include a change in the description of the physics describing the interactions within the detector, an update of the underlying event tune and PDFs
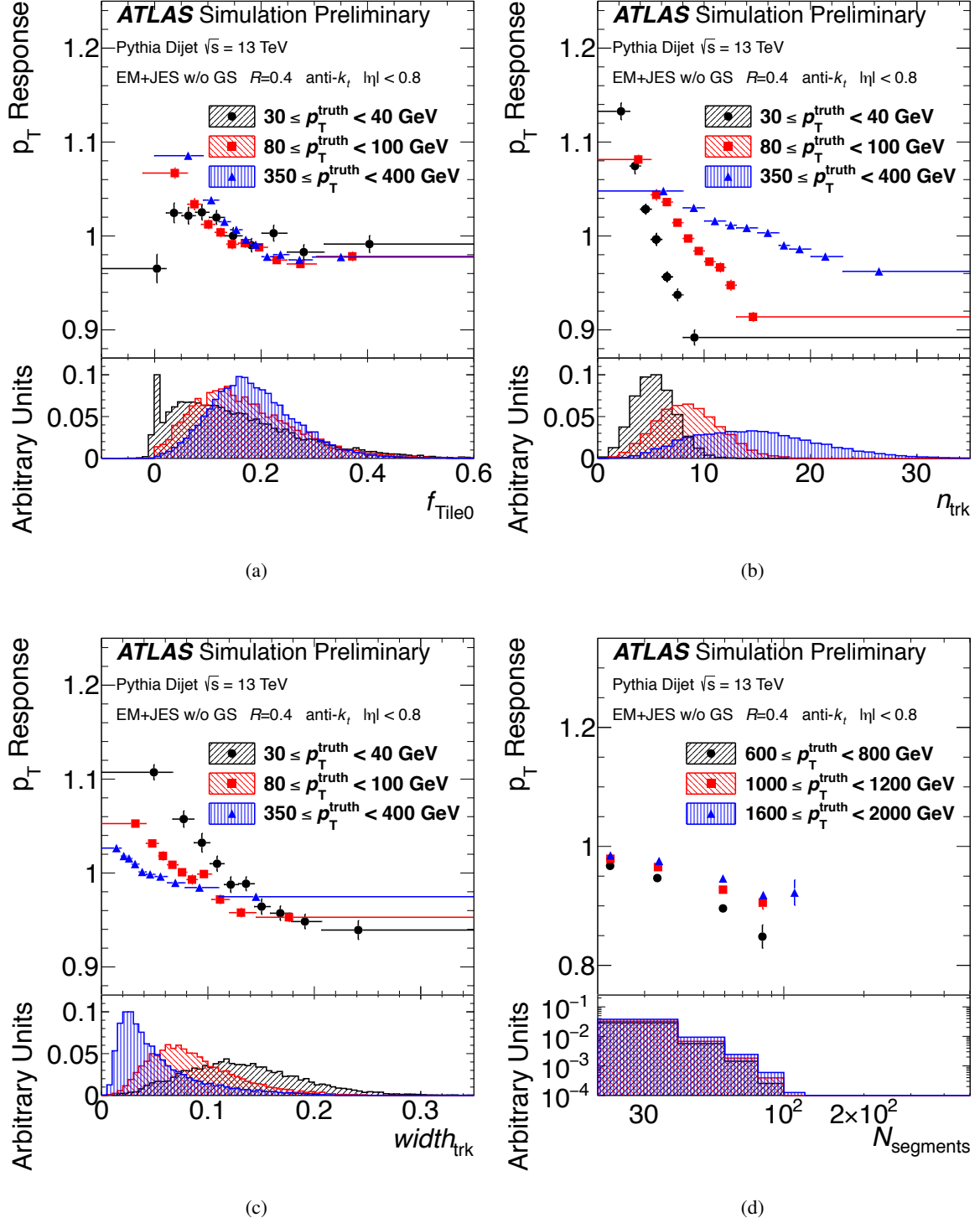
Figure 5: p_T response as a function of the fraction of energy deposited in the first layer of the tile (f_{tile1}) (a), the number of tracks associated to the jet (b), the width calculated with those tracks (c) and the number of muon segments associated to the jet (d), along with the distribution of each variable in the given p_T ranges. All figures correspond to anti-k_t, R=0.4 jets with pile-up and jet energy scale corrections applied matched to a truth jet. Note that plots are shown prior to the application of the global sequential calibration (w/o GS), showing the dependencies that are fit.

and a more accurate description of the ϕ-dependence in the signal reconstruction of the Tile calorimeter. The effects of these changes can be seen in Fig. 6 for the higher of two η bins, $0.3 < |\eta| < 0.8$, in which a correction factor to the 2012 in situ correction is derived by comparing the nominal jet p_T response to samples individually implementing the 2012 condition for each of the 3 changes listed above.
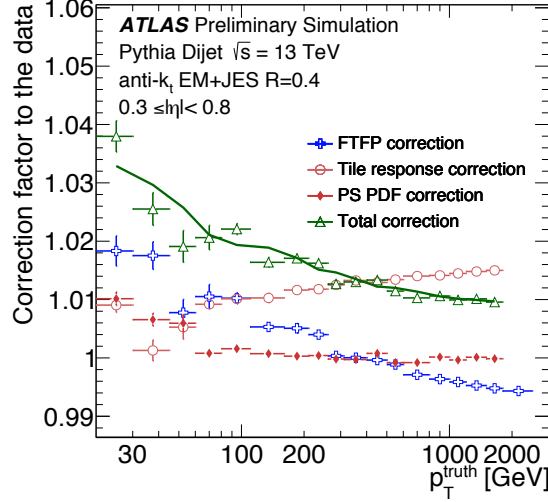

Figure 6: Ratios of the p_T-response used to correct the 2012 in situ correction for anti-k_t $R = 0.4$ jets with $0.3 < |\eta| < 0.8$, as a function of p_T^{truth}. The ratios compare a dijet sample generated using the AU2 tune and CT10 PDF and one with the A14 tune and NNPDF2.0 PDF (red diamonds), a dijet sample generated without ϕ-dependence of the response in the Tile calorimeter and one generated using this ϕ-dependent response (blue crosses), and a dijet sample simulated with the QGSP_BERT physics list and one simulated with the FTFP_BERT list (yellow triangles). The total correction is formed as the product of the three ratios according to Eq. 3 (green empty triangles) and is applied as a smoothed curve (green curve).

These updates in the simulation have no effect on r_{2012}^{data}, but impact the applicability of f_{2012} to 2015 data, because $f_{2012} \times C_{2015} \neq f_{2012} \times C_{2012}$. To correct the calibration factors applied to the data for the changes in detector simulation and MC generator tune and PDFs, f_{2015} is defined as:

$$f_{2015} = \frac{R_{\text{new tune}}}{R_{\text{old tune}}} \times \frac{R_{\text{new tile sim}}}{R_{\text{old tile sim}}} \times \frac{R_{\text{FTFP}}}{R_{\text{QGSP}}} \times f_{2012}, \tag{3}$$

where the three response ratio terms are shown in Fig. 6 and they all depend on p_T and η. The product of the three terms is also shown in Fig. 6.

The use of $f_{2015} \times C_{2015}$ is preferable to the use of $f_{2012} \times C_{2012}$ for 2015 data, because there are certain changes on C in going from 2012 to 2015 that affect both data and MC simulations, for example the changes in the read-out of the LAr calorimeters. This justifies the use of the more complex procedure encapsulated in Eq. 3, which separates out the effects that only impact the MC simulation (which are used to correct f_{2012}) and those that impact both data and MC (which have effects that the MC simulation is assumed to model, within dedicated systematic uncertainties described in Sec. 7).

7 Systematic Uncertainties

Section 6 justified the use of corrections derived in situ in 2012 data to calibrate jets in 2015 data, because such corrections account for differences between MC simulations in 2012 and those in 2015 that are directly applied to 2015 data. This same argument leads to the conclusion that systematic uncertainties derived in situ can be directly applicable to 2015 data. There are a number of changes in the detector and the data-taking conditions that can challenge the validity of this procedure, in particular, most of those described in Sec. 4 (except for the change in hadronic physics, which only affects the MC simulation, as discussed in Sec. 6.4). All these changes are modeled in the MC simulations, but it is reasonable to investigate the degree to which such modeling is accurate and whether the simulation perfectly follows the data.

This section summarizes the studies performed to establish the uncertainties on the jet energy scale and resolution. Section 7.1 summarizes how uncertainties as a function of p_T and η are estimated by quantifying the effect of the different changes described in Sec. 4 in the jet energy scale and resolution. In this section, only jets in the central region of the detector, $|\eta| < 0.8$, are considered for the studies of the jet energy scale as this η range is the necessary input to in situ studies which extend the calibration and derivation of uncertainty to the remaining η range [27]. Jets in the full detector acceptance are considered for studies of the jet resolution. In the following sections jets in the full detector acceptance are studied. Section 7.2 describes the changes that impact the scale dependence on in-time and out-of-time pile-up, and the corresponding systematic uncertainties. Section 7.3 focuses on other uncertainties on the jet energy scale, in particular, those related to the jet flavor and those related to high-p_T jets, as well as uncertainties specific to the global sequential corrections. Finally, Sec. 7.4 shows the total uncertainties and describes how the total number of nuisance parameters are combined into a set of three nuisance parameters to yield uncertainties that capture the main correlations in p_T and η signal regions used by early searches for new physics in 2015 data.

7.1 Uncertainties on p_T and η dependence of jet energy scale and resolution

The changes to experimental conditions are captured in the samples listed in Tab. 1. The changes in jet energy scale and resolution in each of the samples are studied with respect to the reference sample. Changes in scale are taken as additional sources of systematic uncertainty on the in situ correction. Changes in resolution are taken as additional terms in the uncertainty on the the square of the jet resolution as it was calculated in the comparison of 2012 data and MC [2]. It is not necessary to include an uncertainty for the differences between the nominal and reference sample because they do not lead to a difference in jet energy scale and resolution in data. Therefore, since changes that only affect MC have been used in the derivation of an additional factor in the calibration, as detailed in Sec. 6.4, they are found there. The same applies for the study of the QGSP_BERT sample, which has already been studied in Sec. 6.4.

The change in the topoclustering algorithm affects the amount of reconstructed signal and therefore both the jet energy scale and resolution. A similar effect occurs for the change in the noise thresholds. The changes in bunch spacing and sampling reconstruction affect the mapping between the electronic signals and the energy measurements, and have correlated impacts on reconstructed energy. They are studied separately to avoid a potential cancellation of effects and, consequently, an underestimation of the uncertainty. One comparison is made between the energy scale and resolution in 50 ns/5-sampling events, the configuration used in 2012, to that of 50 ns/4-sampling events. This comparison isolates the effects of

the change in the number of read-out samplings. Then, the 50 ns/4-sampling sample is compared to the reference sample, thus isolating the effect of the change in bunch spacing. It may be noted that additional disparities between data and MC could come from the different sampling of the generated pulse shape used in the calibration of LAr calorimeter in Run 2 from that of Run 1. Checks have been performed using reprocessed 2012 data with 4 sample reconstruction that suggest such effects to be only at the level of 0.1%, well within the uncertainty derived from the previously considered changes.

Each one of the comparisons mentioned above, for both the jet energy scale and resolution, are used as additional independent nuisance parameters that are added to those obtained from the in situ studies using 2012 data. The observed changes are the expected effects, as estimated in MC simulations. The inaccuracy of the MC simulations in modeling these changes is expected to be less than the absolute size of the changes, based on the many Run 1 studies demonstrating the high quality of the simulation. Therefore, the use of the absolute size of the observed changes may be an over estimate of the uncertainty associated with them.

Each difference between samples has been taken as an additional uncertainty propogated in quadrature for the jet energy scale. In contrast, the signed square root of the difference of the squares of the resolutions, or *smearing factor*, is used for the augmentation of jet energy resolution to correctly add to the total variance the terms from these additional uncertainties. Jets in analyses are smeared with the systematic uncertainties derived from in situ studies on 2012 data [2]. The smearing factors derived within this note are combined with the aforementioned to account for any potential effects on the resolution from the changes in detector conditions that may not be properly simulated in 2015 MC.

Additionally, to capture the differences in the underlying event tune an additial systematic uncertainty is made from the comparison of the reference and nominal sample (with the ϕ-dependent Tile simulation turned off to match the reference sample). This comparison has already been discussed in Sec. 6.4 and the difference has been used as a correction to the 2012 in situ calibration. Here it does not represent a change in the data in going from 2012 to 2015, but rather an uncertainty in the MC modeling of the underlying event in 2015 data due to the increase in center-of-mass energy. The difference between these two samples is therefore taken to be a conservative estimate of the systematic uncertainty of the extrapolation of the underlying event from $\sqrt{s} = 8$ TeV to $\sqrt{s} = 13$ TeV. Any deviation from the expected performance due the application of the simulated underlying event tuned to $\sqrt{s} = 8$ TeV ATLAS data to data taken at $\sqrt{s} = 13$ TeV should be amply captured by the difference between this tune and its predecessor.

The relative change in jet energy scale and resolution smearing factor for all the previously mentioned comparisons is shown in Fig. 7 for the $0.3 < |\eta| < 0.8$ bin. The effects of the different data-taking conditions studied are most prominent at low p_{T} and are negligible for jets of $p_{\mathrm{T}} > 200$ GeV. The difference between the "early data" conditions sample and the reference sample is also shown. This difference is used as an additional uncertainty for data taken with 50 ns bunch spacing in 2015. It is also used as an additional uncertainty in the $|\eta| > 0.8$ region for 25 ns data, given that the nominal uncertainties are obtained using data collected in June $7^{\mathrm{th}} - 15^{\mathrm{th}}$ with a bunch spacing of 50 ns [27] but applied to 25 ns data.

Since the studies of the jet energy scale in this section focus on jets with $|\eta| < 0.8$, the sample with a modified description of the forward region material is not shown in Fig. 7. Therefore this sample is only relevant for the study of the jet resolution. Figure 8 shows the change in resolution between this sample and the reference sample in two forward η bins, which is used as an additional nuisance parameter in the jet resolution systematic uncertainties. The changes derived from comparisons between the other relevant samples are also shown.
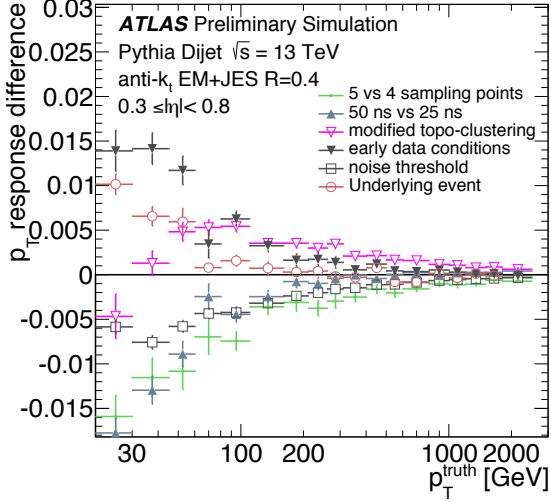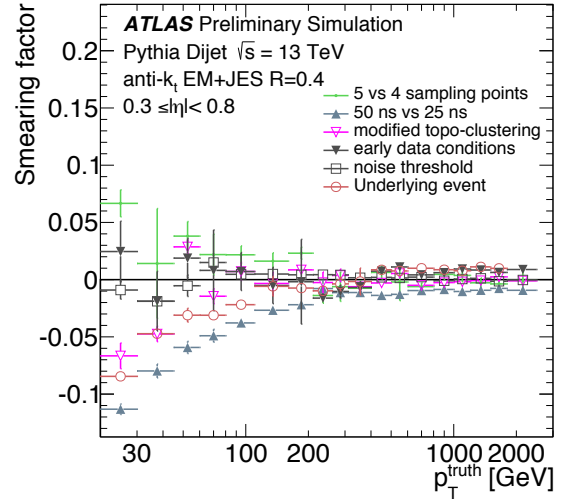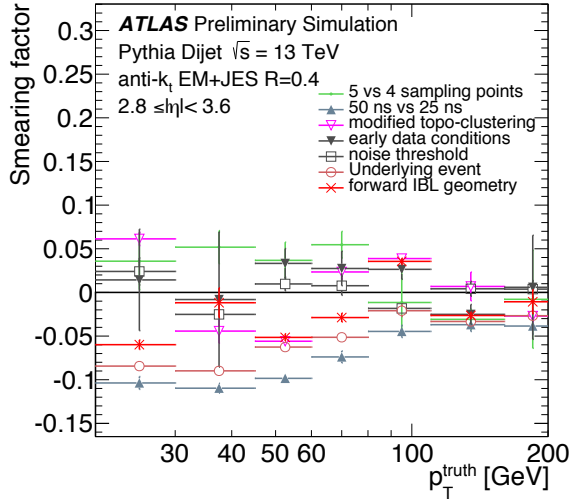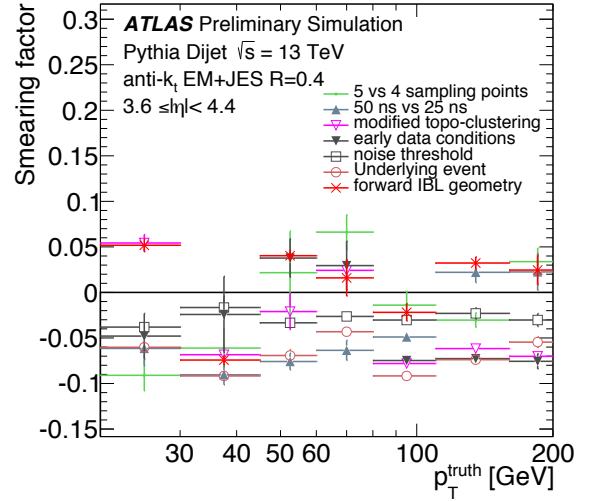
Figure 7: Relative change in jet energy scale (a) and resolution smearing factor (b) for different comparisons used to estimate the additional systematic uncertainties in 2015 data for jets with $0.3 < |\eta| < 0.8$.

Figure 8: Jet resolution smearing factors derived from different comparisons used to estimate the additional systematic uncertainties on the jet resolution in 2015 data for jets with $2.8 < |\eta| < 3.6$ (a) and $3.6 < |\eta| < 4.4$ (b).

7.2 Uncertainties dependent on pile-up conditions

Pile-up dependent uncertainties are also determined from in situ studies made in 2012 [28], with a similar strategy as taken above to apply them to 2015 data. Systematic contributions orginating purely from MC simulation have been recalculated and differences in conditions between 2012 and 2015 are taken into account as additional sources of uncertainty. The pile-up uncertainty is split into four components that account for potential mismodelings associated to the $N_{\rm PV}$ and μ dependence of the average MC-based residual pile-up correction, the $p_{\rm T}$-dependence of this residual correction, and the dependence of ρ on the event topology.

Some of the effects described in the previous section may change the jet energy by a magnitude that depends on the amount of in-time and out-of-time pile-up activity in an event. The use of the $\rho \times A$ correction (described in Sec. 6.1), cancels such effects to first order, but a remaining dependence on these changes may persist into the pile-up residual correction. The uncertainty associated with the residual pile-up dependence on changes between 2012 and 2015 is quantified by taking the difference in residual corrections between the reference sample and five other samples over the full η-range of the calorimeter, preserving the η dependence of those differences. The reference sample is compared to the early 2015 data-taking conditions sample with 50 ns bunch spacing to account for changes in the data-taking conditions, two comparisons are made with thresholds varied up and down in order to account for updated noise thresholds and potential changes in the pile-up contributions due to the change in the center-of-mass energy of the collisions, a comparison is made to the Run 1 topoclustering sample to capture any changes resulting from the updated algorithm, and finally to account for the IBL services the sample with ϕ-modulated description of the geometry of the IBL services in the forward region was compared to the reference sample. Figure 9 shows these differences for the residual correction as a function of the amount of in-time pile-up (a) and out-of-time pile-up (b), where in each case the η-range has been limited to that affected by the change.

Uncertainties on the residual pile-up term depend linearly on $N_{PV} - N_{PV}^{\rm ref}$ and $\mu - \mu^{\rm ref}$, where the reference values are those at which the in situ tests were performed with the average μ and N_{PV} found in 2012 data. These variables are comparable in 2015 MC simulations, which means that, on average, these uncertainties are 0. Therefore, no double-counting is incurred in using the same samples for the $p_{\rm T}$ and η-dependent uncertainties and the pile-up residual uncertainties, since they capture two different effects: the effect on the average jet energy scale (Sec. 7.1) and the effect on the dependence of the jet energy scale on pile-up activity. Unlike for the uncertainties described in Sec. 7.1, no additional nuisance parameters are added to the jet energy scale systematic uncertainties. Instead, the differences between the samples are added in quadrature with the uncertainties derived in situ with 2012 data to provide updated uncertainties on the pile-up residual term for 2015 data.

The $p_{\rm T}$-dependent uncertainty is calculated from the 2015 dijet sample and accounts for the fact that the residual effects are not independent of the jet $p_{\rm T}$. In situ tests in 2012 have shown that such effects are well-modeled by MC simulations [28], but the studies have large statistical uncertainties. For this reason, the full size of the effect in MC simulation is used as an additional systematic uncertainty. This effect has been studied in the 2015 nominal sample and is shown in Fig. 10. As for 2012 data analyses, this full effect is taken as an additional systematic uncertainty.

Lastly, the topology uncertainty arises from the fact that the mean value of ρ was found to be different in different topologies at fixed N_{PV}, and that difference was not modeled correctly in 2012 MC simulations [28]. This uncertainty is not expected to change significantly in 2015 data, given its correlation with
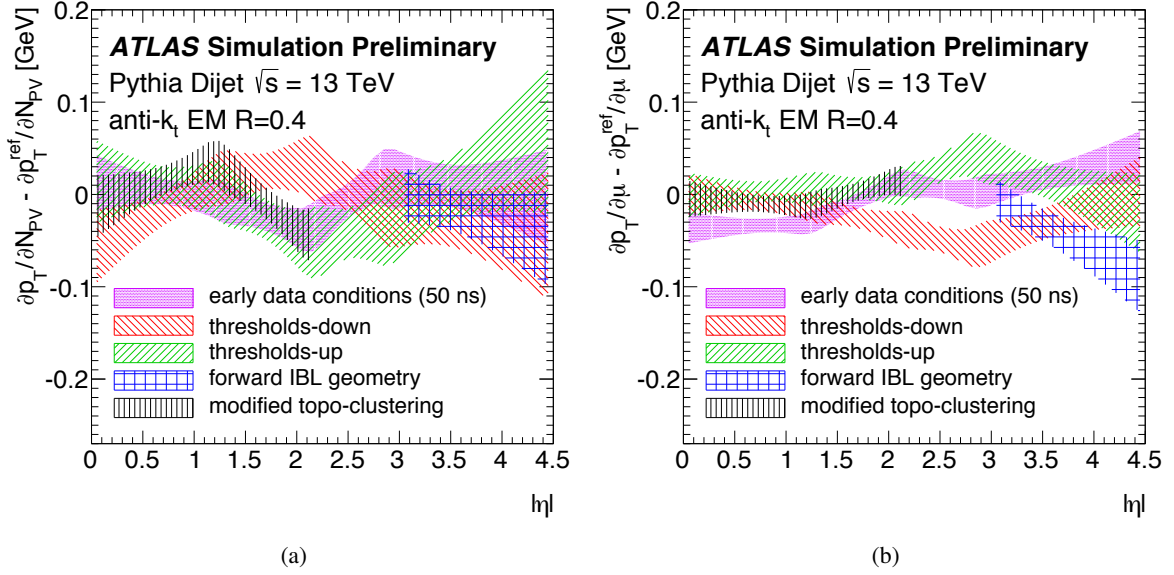
(a)

(b)

Figure 9: The difference in fits made to the residual pile-up dependence for various samples compared to the reference sample for in-time (a) and out-of-time (b) pile-up, drawn in 1-σ error bounds calculated from the fitting procedure. Each sample comparison is used as an additional source of N_{PV} and $\langle\mu\rangle$-dependent systematic uncertainty in 2015 data as a function of $|\eta|$.
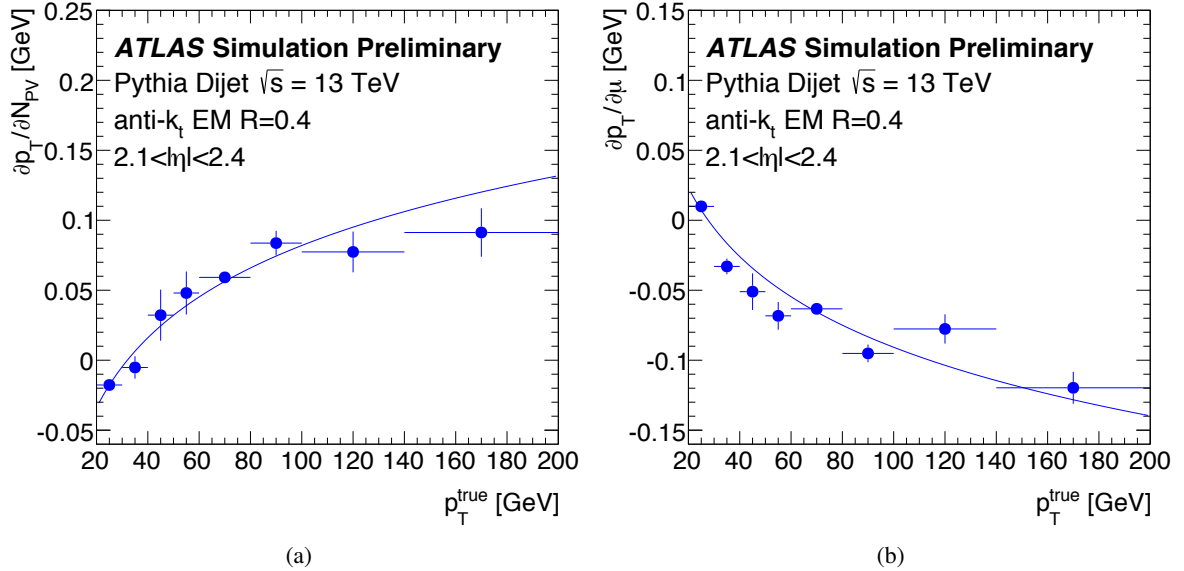

(a)

(b)

Figure 10: p_T-dependence of the residual term on in-time (a) and out-of-time (b) pile-up for jets of $2.1 < |\eta| < 2.4$ after all pile-up corrections have been applied in the nominal MC sample, showing the fit logarithmic dependence.

the physical processes producing different types of events in collisions recorded by the ATLAS detector. For this reason, the same value as used in 2012 is used for the analysis of early 2015 data.

7.3 Other uncertainties: flavor, global sequential corrections and high p_{T}

Since the in situ uncertainties rely on analyses performed in data samples with a specific jet flavor composition, three additional uncertainties associated with flavor are estimated: one specific to *b*-jets, one specific to gluon jets and one that captures the effect on the jet energy scale caused by the uncertainty on the flavor composition of a given analysis sample. In 2012 analyses, these uncertainties were estimated using MC simulations [26]. The gluon jet energy scale uncertainty (referred to as "flavor response" uncertainty) was calculated through comparisons of the jet energy scale of jets labeled as gluons in Herwig++ and Pythia 8. The "flavor composition" uncertainty was calculated taking into account the difference in jet energy scale of jets labeled as gluons or light quarks in a Pythia 8 dijet sample. These two uncertainties have been recalculated using the reference sample and its comparison to the Herwig++ sample and are shown in Fig. 11 for jets in the central region of the detector. These results are of equivalent size to those
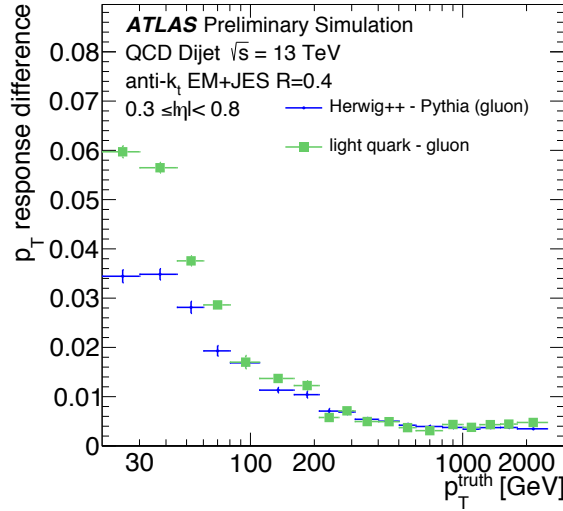
Figure 11: Difference in response between jets labeled as light quark and gluon jets (blue) in a Pythia 8 dijet sample and between gluon jets in the same Pythia 8 dijet sample and a Herwig++ dijet sample (green) for jets with $|\eta| < 0.8$.

observed in Ref. [26] with 2012 MC simulations, demonstrating the very small sensitivity of this type of uncertainties to the changes undergone by the ATLAS experiment for Run 2 data. For this reason, the uncertainty specific to *b*-jets is not recalculated and instead the one derived using 2012 MC simulation is used.

The addition of the IBL and corresponding changes in tracking suggest that special care may be needed to understand systematic uncertainties due to these upgrades. The global sequential corrections benefitting from tracking upgrades have been recalculated (see Sec. 6.3) to use the new reconstruction and do not change the average p_{T} response of jets in the calibration sample. Furthermore, tracking in this case is just a proxy for the effect of jet fragmentation on the jet energy scale. Since that effect remains unchanged, the only relevant question is whether the level of agreement between data and MC simulations in the variables

used by the global sequential corrections remain the same in 2015 data as in 2012 data [15]. This has been demonstrated in early 2015 data studies [14] and justifies the addition of no additional systematic uncertainties due to the tracking-based global sequential corrections.

A similar question arises when considering uncertainties on the correction that depends on the number of reconstructed muon segments behind the jet. Similar arguments to those made about tracking can be made in this case. However, not enough data exist in very early data analyses to establish the level of agreement between MC and data at the jet p_T region for which this correction is most relevant for $p_T > 1$ TeV. For this reason, the maximum difference between data and MC measured in 2012 data [15] in the jet response as a function of the number of segments is taken as a systematic uncertainty for all jets that have this correction applied.

Finally, the in situ methods described in Ref. [26] are only capable of reaching jet p_Ts up to 1.8 TeV. For jets of higher p_Ts, the jet energy scale is estimated from the response of single hadrons. Jets are treated as a superposition of the individual energy deposits of their constituent particles as described in Ref. [11]. No special treatment is required for this region of phase space, beyond the addition of the uncertainties due to jets not fully contained in the calorimeter discussed in the previous paragraph.

7.4 Reduction of nuisance parameters and summary of uncertainties

The list of uncertainties described above requires an analysis to propagate a total of 74 jet energy scale uncertainty terms to correctly account for all correlations in the jet calibration. For many analyses it is preferable to describe such correlations using a reduced set of nuisance parameters. The procedure described in Ref. [26, 29] is repeated with the additional nuisance parameters described in Sec. 7.1. One reduction scheme with minimal loss of correlation is provided that reduces the number of in situ (and additional p_T-dependent) nuisance parameters from 61 to 6, resulting in a total of 18 nuisance parameters. Furthermore, following the procedure described in Ref. [31], 4 sets of uncertainties each with 3 nuisance parameters are derived. A significant loss of correlation information is observed in all these sets of uncertainties, but the correlation loss affects different parts of parameter space in each set, allowing analyses to test their sensitivity to the correlations in the jet energy scale uncertainties by changing from one set to another.

In the case of the jet energy resolution, the uncertainties derived in Sec. 7.1 are dominant and have a similar shape. For this reason all uncertainties are combined into one nuisance parameter to be propagated in a correlated way. The combination of the this additional uncertainty with the 2012 in situ uncertaities is shown in Fig. 12.

Figure 13 summarizes the main contributions to the total jet energy scale uncertainties for jets in the central region of the detector. Two bands are shown, corresponding to the final 2012 uncertainties reported in Ref. [26] and the total updated uncertainties for early 2015 data. In addition, curves are shown for the contributions from pile-up, flavor, 2012 in situ analyses and the contributions estimated in Sec. 7.1. Uncertainties are shown under the assumption of no knowledge of flavor composition in the analysis. The total uncertainty is shown for the nominal data taking period with 25 ns bunch spacing (a) and the early data taking period with 50 ns bunch spacing (b).
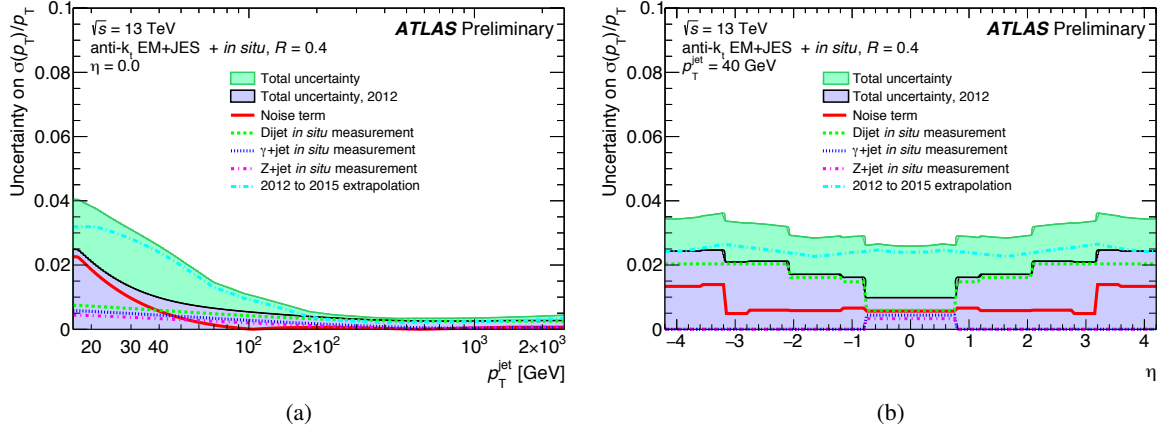
Figure 12: Final jet energy resolution uncertainties estimated for 2015 data with 25 ns bunch spacing as a function of jet p_T for jets of $\eta = 0$ (a) and as a function of η for jet p_T of 40 GeV (b).
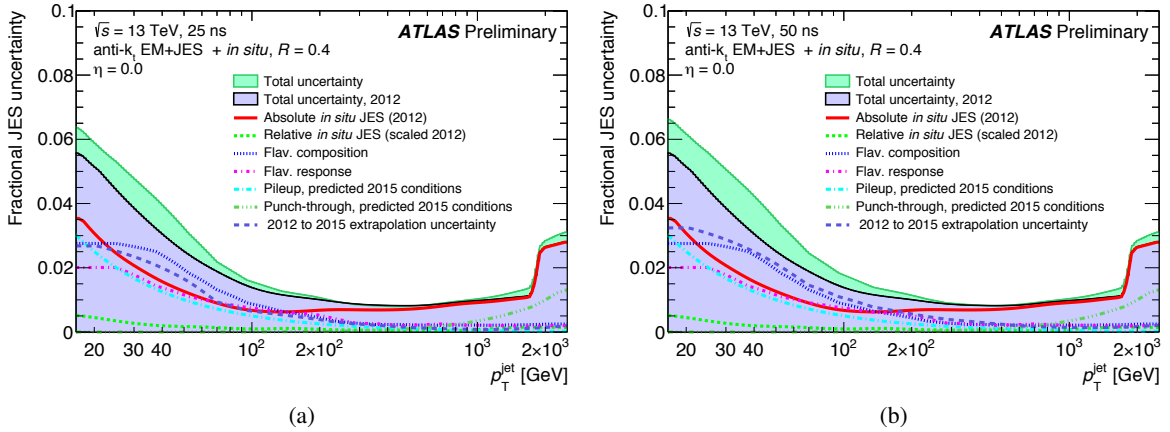

Figure 13: Final jet energy scale uncertainties estimated for 2015 data as a function of jet p_T for jets of $\eta = 0$. Uncertainties are shown under the assumption of no knowledge of flavor. The total uncertainty is shown for the nominal data taking period with 25 ns bunch spacing (a) and the early data taking period with 50 ns bunch spacing (b).

8 Conclusions

This document has described the calibration of $R = 0.4$ anti-k_t jets reconstructed in the ATLAS detector at a center-of-mass energy of 13 TeV. It has also described how systematic uncertainties on the jet energy scale and resolution have been derived exploiting knowledge acquired during Run 1 combined with detailed studies using MC simulations. These MC simulations describe the individual changes in detector and data taking conditions that the ATLAS detector has experienced in transition from the 2012 data taking period to the 2015 data taking period. In this way, the impact of each change on the jet energy scale and resolution has been evaluated. That impact has been conservatively used to establish a systematic uncertainty caused by each effect. In the case of the jet resolution, these effects dominate the uncertainties. In the case of the jet energy scale, they are subdominant, and have been treated as independent terms contributing to the total jet energy scale uncertainty, derived using 2012 data analyses. The techniques developed in Run 1 have then been used to reduce the total number of jet energy scale uncertainty terms to 3 for thoseanalyses unaffected by the loss in correlation. The full set of systematic uncertainties for the jet energy scale has been presented for jets with $|\eta| < 0.8$. These uncertainties vary from 6% for jets of $p_T = 20$ GeV, decreasing to 1% for jets of $p_T = 200 - 1800$ GeV and increasing to 3% for jets of higher p_T, for the average pile-up conditions expected during the 2015 data-taking period. Uncertainties on the jet resolution and also those related to how pile-up affects the jet energy scale have been derived for the full η range of the detector.

References

[1] ATLAS Collaboration, *The ATLAS Experiment at the CERN Large Hadron Collider*, JINST **3** (2008) S08003.

[2] ATLAS Collaboration, *Data-driven determination of the energy scale and resolution of jets reconstructed in the ATLAS calorimeters using dijet and multijet events at sqrt(s)=8 TeV*, ATLAS-CONF-2015-017 (2015), URL: https://cds.cern.ch/record/2008678.

[3] ATLAS Collaboration, *ATLAS Insertable B-Layer Technical Design Report*, CERN-LHCC-2010-013. ATLAS-TDR-19 (2010), URL: https://cds.cern.ch/record/1291633.

[4] H. Abreu, *Performance of the electronic readout of the ATLAS liquid argon calorimeters*, Journal of Instrumentation **5**.09 (2010) P09003, URL: http://stacks.iop.org/1748-0221/5/i=09/a=P09003.

[5] ATLAS Collaboration, *Readiness of the ATLAS Tile Calorimeter for LHC collisions*, Eur.Phys.J. **C70** (2010) 1193–1236, arXiv: 1007.5423 [physics.ins-det].

[6] J. Saraiva, *Commissioning of the ATLAS tile calorimeter with single beam and first collisions*, Nucl.Phys.Proc.Suppl. **215** (2011) 107–109.

[7] S. Artz et al., *Upgrade of the ATLAS Central Trigger for LHC Run-2*, JINST **10**.02 (2015) C02030.

[8] H. Ma, *Upgraded Trigger Readout Electronics for the ATLAS LAr Calorimeters for Future LHC Running*, J.Phys.Conf.Ser. **587**.1 (2015) 012019.

[9] M. Cacciari, G. P. Salam and G. Soyez, *The Anti-k(t) jet clustering algorithm*, JHEP **0804** (2008) 063, arXiv: 0802.1189 [hep-ph].

[10] ATLAS Collaboration, *Jet energy scale and its systematic uncertainty in proton-proton collisions at sqrt(s)=7 TeV with ATLAS 2011 data*, ATLAS-CONF-2013-004 (2013), URL: https://cds.cern.ch/record/1509552.

[11] ATLAS Collaboration, *Jet energy measurement with the ATLAS detector in proton-proton collisions at sqrt(s)=7 TeV*, Eur.Phys.J. **C73**.3 (2013) 2304, arXiv: 1112.6426 [hep-ex].

[12] M. Cacciari, G. P. Salam and G. Soyez, *The Catchment Area of Jets*, JHEP **0804** (2008) 005, arXiv: 0802.1188 [hep-ph].

[13] ATLAS Collaboration, 'Optimisation of the ATLAS Track Reconstruction Software for Run-2', tech. rep. ATL-SOFT-PROC-2015-056, CERN, 2015, URL: https://cds.cern.ch/record/2018442.

[14] ATLAS Collaboration, *Properties of Jets and Inputs to Jet Reconstruction and Calibration with the ATLAS Detector Using Proton-Proton Collisions at sqrt(s) = 13 TeV*, ATL-COM-PHYS-2015-376 (2015), URL: https://cds.cern.ch/record/2014750.

[15] ATLAS Collaboration, *Jet global sequential corrections with the ATLAS detector in proton-proton collisions at sqrt(s) = 8 TeV*, ATLAS-CONF-2015-002 (2015), URL: https://cds.cern.ch/record/2001682.

[16] ATLAS Collaboration, *Measurement of the muon reconstruction performance of the ATLAS detector using 2011 and 2012 LHC proton-proton collision data*, Eur.Phys.J. **C74**.11 (2014) 3130, arXiv: 1407.3935 [hep-ex].

[17] ATLAS Collaboration, *Light-quark and gluon jet discrimination in pp collisions at $\sqrt{s}$ = 7 TeV with the ATLAS detector*, Eur.Phys.J. **C74**.8 (2014) 3023, arXiv: 1405.6583 [hep-ex].

[18] Apostolakis, J., Dotti, A., Folger, G., Ivanchenko, V., Kosov, M., Ribon, A., Uzhinsky, V. and Wright, D., *Status of Geant4 hadronic physics for the simulation of LHC experiments at the start of LHC physics program*, CERN-LCGAPP **2** (2010) 2.

[19] T. Sjostrand, S. Mrenna and P. Z. Skands, *A Brief Introduction to PYTHIA 8.1*, Comput.Phys.Commun. **178** (2008) 852–867, arXiv: 0710.3820 [hep-ph].

[20] ATLAS Collaboration, *ATLAS Run 1 Pythia8 tunes*, ATL-PHYS-PUB-2014-021 (2014), URL: http://cds.cern.ch/record/1966419.

[21] J. Pumplin et al., *New generation of parton distributions with uncertainties from global QCD analysis*, JHEP **0207** (2002) 012, arXiv: hep-ph/0201195 [hep-ph].

[22] ATLAS Collaboration, *The ATLAS Simulation Infrastructure*, Eur.Phys.J. **C70** (2010) 823–874, arXiv: 1005.4568 [physics.ins-det].

[23] S. Agostinelli et al., *GEANT4: A Simulation toolkit*, Nucl.Instrum.Meth. **A506** (2003) 250–303.

[24] H.-L. Lai et al., *New parton distributions for collider physics*, Phys.Rev. **D82** (2010) 074024, arXiv: 1007.2241 [hep-ph].

[25] A. Buckley et al., *General-purpose event generators for LHC physics*, Phys.Rept. **504** (2011) 145–233, arXiv: 1101.2599 [hep-ph].

[26] ATLAS Collaboration, *Monte Carlo Calibration and Combination of In-situ Measurements of Jet Energy Scale, Jet Energy Resolution and Jet Mass in ATLAS*, ATLAS-CONF-2015-037 (2015), URL: https://cds.cern.ch/record/2044941.

[27] ATLAS Collaboration, *In-situ determination of the ATLAS forward jet energy scale and uncertainty using dijet events at sqrt(s) = 13 TeV*, ATLAS-COM-CONF-2015-023 (2015), URL: https://cds.cern.ch/record/2015470.

[28] ATLAS Collaboration, *Pile-up subtraction and suppression for jets in ATLAS*, ATLAS-CONF-2013-083 (2013), URL: https://cds.cern.ch/record/1570994.

[29] ATLAS Collaboration, *Jet energy measurement and its systematic uncertainty in proton-proton collisions at sqrt(s)=7 TeV with the ATLAS detector*, Eur.Phys.J. **C75**.1 (2015) 17, arXiv: 1406.0076 [hep-ex].

[30] ATLAS Collaboration, *Determination of the jet energy scale and resolution at ATLAS using Z/photon-jet events in data at sqrt(s)=8 TeV*, ATL-COM-PHYS-2014-791 (2014), URL: https://cds.cern.ch/record/1741697.

[31] ATLAS Collaboration, *Minimal representations of ATLAS experimental uncertainties*, ATL-COM-PHYS-2015-374 (2015), URL: https://cds.cern.ch/record/2014656.